Miniaturized Dual-Band Broadside/Endfire Antenna-in-Package for 5G Smartphone

Jungwoo Seo, Inseop Yoon, *Member, IEEE*, Jaebaek Jung, *Member, IEEE*, Jeongki Ryoo, Juhyoung Park, Woncheol Lee, *Member, IEEE*, Dongok Ko, and Jungsuek Oh, *Senior Member, IEEE*

***Abstract*— This article proposes a miniaturized antenna in package (AiP) for 5G millimeter-wave smartphone that incorporates broadside and endfire arrays and supports a dual band covering 28 and 39 GHz. This article demonstrates that the proposed AiP is 5.8 mm × 19 mm × 1.122 mm. It is believed that this is the smallest 5G AiP that can support a 10 dBi antenna gain, a 10 dB return-loss bandwidth of 3 GHz, and more than 10 dB isolation for both broadside and endfire arrays. AiP consists of a 1 × 4 patch antenna array for broadside radiation and a 1 × 4 dipole antenna array for endfire radiation. To miniaturize the patch antenna elements, a multilayer Reactive Impedance Surface (RIS) is embedded between the patch layer and the ground plane. This multilayer RIS idea greatly fits in 5G PCB-stack-up antennas where each stack-up layer essentially requires certain portion of copper area. For the endfire array antenna, miniaturization with bandwidth improvement is achieved by modifying the vertically bent folded dipole antenna (VBFDA) and adding a tightly coupled T-shape side via wall. The AiP achieves a 10 dB return-loss bandwidth of 26.22 to 29.57 GHz and 35.18 to 41.00 GHz for Multilayer RIS Patch Antenna (MLRPA), and 26.40 to 29.74 GHz and 36.65 to 40.72 GHz for VBFDA. The antenna gain is 11.6 dBi for MLRPA and 10.0 dBi for VBFDA.**

***Index Terms*— 5G, antenna miniaturization, impedance sheets, millimeter-wave antenna arrays, packaging.**

I. Introduction

THE fifth-generation (5G) is a big evolution for mobile communication systems, which was first commercialized in 2019. 5G frequency bands contain sub-6 GHz (3.5 GHz) and millimeter-wave (mmWave) frequency bands. Recently, Federal Communications Commission (FCC) recommended new regulations to manage 28, 37, 39, and 64–71 GHz frequency bands for 5G applications. Among these, 28 and 39 GHz are the most dominant frequency bands that are used by major service providers in the world [1]. From these, mmWave dual-band operations are being a key requirement for antennas and front-end module (FEM) in advanced 5G systems. In addition to this, there is also a demand for dual-polarized mmWave systems to acquire a diversity gain for various emerging services [2], [3]. Designing antennas for 5G smartphones is one of the most challenging issues because large display size and thin frame significantly reduce the space for 5G antennas. This renders the design freedom in achieving broadband and beam steering capabilities with a moderate antenna gain. Qualcomm developed and announced a 5G antenna module [4] and a significant number of studies have been performed [5]–[11]. However, the gain, bandwidth, and size of the antennas for 28 and 39 GHz operations are impractical for smartphones. Various types of dual-band, dual-polarized, and miniaturized antennas using patch or dipole antennas have been widely researched; however, most of these antennas have drawbacks. Studied patch antennas are not small, they do not support dual-band technology, or they do not support dual-polarization [5]–[7]. Similarly, studied dipole antennas are also not small or do not support dual-band technology [10], [11]. Even if some of the studied antennas support dual band and dual polarization simultaneously [8], [9], their size is still unrealistic to be integrated into 5G products.

To clarify the present state-of-the-art, Table I indicates that the most studied designs do not support dual polarization and dual band, nor have a miniaturized size simultaneously. In addition, their performance is not enough to be applied for commercial mmWave 5G smartphones. In the conventional designs, antenna miniaturization in size and profile for both broadside and endfire antenna arrays causes a substantially decreased gain and bandwidth. To address this, there are several types of reactive impedance surfaces (RIS), such as multiband RIS [12], reconfigurable RIS [13], and the RIS cavity resonator [14]. By inserting a conventional single-layer RIS between the patch and the ground, these antennas have a wider bandwidth and a miniaturized size. However, these approaches are difficult to control the resonant frequencies and it needs a higher level of miniaturization to be mounted in a smartphone. In addition, several types of dipole antennas have been studied in related works [10], [11]. These studies have relied mainly on bending arms of the dipole for antenna miniaturization. Likewise, these approaches are difficult to

Manuscript received July 7, 2020; revised April 10, 2021; accepted April 29, 2021. Date of publication June 16, 2021; date of current version December 16, 2021. This work was supported in part by the Samsung Electro-Mechanics and in part by the Institute of Information and Communications Technology Planning and Evaluation (IITP) grant funded by the Korea Government (MSIT), Millimeter-wave Metasurface-based Dual-band Beamforming Antenna-on-Package Technology for 5G Smartphone under Grant 2020-0-00858. *(Corresponding author: Jungsuek Oh.)*

Jungwoo Seo, Jaebaek Jung, and Jungsuek Oh are with the Department of Electrical and Computer Engineering, Institute of New Media and Communications (INMC), Seoul National University, Seoul 08826, South Korea (e-mail: jw.seo@snu.ac.kr; holdmyhand0694@gmail.com; jungsuek@snu.ac.kr).

Inseop Yoon is with the Department of Electronic Engineering, Inha University, Incheon 22201, South Korea (e-mail: lunarmaestro@inha.edu).

Jeongki Ryoo, Juhyoung Park, Woncheol Lee, and Dongok Ko are with Samsung Electro-Mechanics, Suwon 443743, South Korea (e-mail: jeongki.ryoo@samsung.com; blueq@samsung.com; woncheol.lee@samsung.com; dongok.ko@samsung.com).

Color versions of one or more figures in this article are available at https://doi.org/10.1109/TAP.2021.3088230.

Digital Object Identifier 10.1109/TAP.2021.3088230

TABLE I
COMPARISON OF THE PROPOSED AiP TO OTHER ANTENNA STUDIES

Ref. No.	Antenna Type	Number of elements	Size [mm]	Operating frequency (Bandwidth) [GHz]	Peak Gain [dBi]	Dual band / Dual polarization
[5]	Patch	1 × 4	27.5 × 40 × 0.254	27.95-28.27 (0.32) / 37.29–39.19 (1.9)	11.9 / 11.2	Y / N
[6]	Patch	1 × 4	27.5 × 28.5 × 0.661	26.71-30.36 (3.65) / 36.59-38.78 (2.19)	10.06 / 10.2	Y / N
[7]	Patch	3 × 2	35 × 25 × 1.575	25.80-30.23 (4.43) / 35.90-39.44(3.54)	7.47 / 12.1	Y / N
[8]	Patch	1 × 8	47.7 × 10 × 0.387	27.88-28.28 (0.4) / 38.56-39.28 (0.72)	15.2 / 16.9	Y / Y
[9]	Dipole	1 × 1	6 × 8 × 0.254	26.98-29.81 (2.83) / 34.29-42.20 (7.91)	4.0 / 4.63	Y / N
[10]	Dipole	1 × 8	44 × 1.2 × 1.524	25-33 (8)	13	N / N
[11]	Dipole	1 × 8	38.4 × 5.8 × 0.254	26.5-38.2 (11.7)	12.5	N / N
This Study	Patch	1 × 4	19 × 4.4 × 1.122	26.22-29.57 (3.35) / 35.18-41.00 (5.85)	10.5 / 11.9	Y / Y
	Dipole	1 × 4	19 × 1.2 × 1.122	26.40-29.74 (3.34) / 36.65-40.72 (4.07)	8.7 / 10.0	Y / N

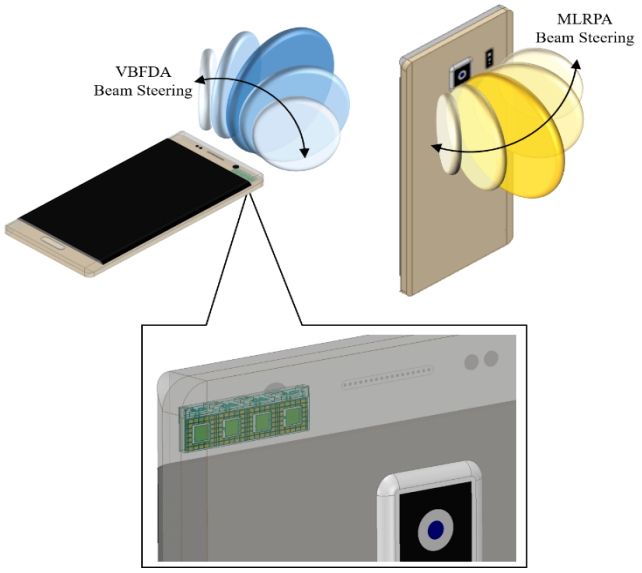

Fig. 1. Proposed AiP topology incorporating MLRPA for broadside radiation and VBFDA for endfire array radiation.

achieve the desired bandwidth, a moderate level of isolation among all of the ports, and require a small form factor for the AiP. The proposed AiP consists of a 1 × 4 multilayer RIS patch antenna (MLRPA) array, and a 1 × 4 vertically bent folded dipole antenna (VBFDA) array. It is a laborious task to achieve various functions of AiP without performance degeneracy when AiP is mounted in very limited smartphone mounting space. Nevertheless, proposed AiP can achieve dual band, dual polarization, a moderate antenna gain, isolation using via wall, and wide bandwidth characteristics with the smallest form factor of 5.8 mm × 19 mm × 1.122 mm (=0.54 λ_0 × 1.76λ_0 × 0.105λ_0, where λ_0 is the free-space wavelength at 28 GHz), as illustrated in Fig. 1.

Section II describes the overall structure and design considerations of the AiP. Section III introduces the proposed feed network, design methodology of the RIS, and the operating principles of MLRPA. The proposed MLRPA array employs multilayer RIS that can maximize the effect of RIS for an extremely small-sized antenna meeting PCB stack-up requirements. Section IV shows the principle of VBFDA by using side via walls. To miniaturize the dipole antenna size and to achieve dual-band operations, the proposed VBFDA array employs vertically folded arms. This study also proposes that the T-shaped side via walls that are placed between the dipole antennas in the VBFDA array can improve isolation and impedance matching. The package-level simulation and the measurement results are presented in Section V. Finally, the conclusion is presented in Section VI.

II. WHOLE CONFIGURATION OF AiP

Fig. 2 depicts the proposed AiP consisting of a 1 × 4 patch antenna array with a multilayer RIS and a 1 × 4 vertically folded bent dipole antenna array with a T-shaped side via walls. The total size, including the solder resist (SR) layer, is 5.8 mm × 19 mm × 1.122 mm. The size of the MLRPA is 4.4 mm × 19 mm × 0.719 mm and the VBFDA is 1.2 mm × 19 mm × 1.122 mm. The two antennas are divided by a ground via wall with a thickness of 0.2 mm. Fig. 2(a) indicates the total view of the proposed AiP and detail of end fire (EF) side via wall that consists of copper via and pads. Pads are inserted in layers 1∼6, 7∼12, and via interconnect pads. Fig. 2(b) is the top view of the proposed AiP, it portrays the location of MLRPA, VBFDA ports, and broad side (BS) RIS. Ports of x-pol and y-pol of MLRPA are under the BS patch and BS RIS surrounds these elements. VBFDA ports are under the BS RIS and are connected to the dipole arm through a stripline. Fig. 2(c) is the side view of the proposed AiP that shows BS RIS and BS/EF via wall whose structure is equal to EF side via wall. Detailed explanations of BS RIS are covered in Section III-A. Fig. 2(d) and Fig. 2(c) are similar in the sense that these figures are the side view of AiP. For a clear understanding of feeding line structure, however, Fig. 2(d) depicts the side view of AiP without RIS and EF side via wall. The detailed explanations of the feeding line structure are also covered in Section III-A.

The stack-up structure of the 12-layer PCB lamination being widely used for 5G antennas is illustrated in Fig. 3. The permittivity and loss tangent of the preimpregnated (prepreg) material and the SR layer are 3.47, 0.004 and 3.9, 0.03, respectively. The 12 layers are stacked up and down based on the core prepreg material. Copper layers of the MLRPA are placed on layer 1 to layer 7. The radiating patches are placed on layer 1, the RIS is on layers 1 to layer 6, and the ground antenna is on layer 7. Layers 7 to 9 place the strip lines along the top

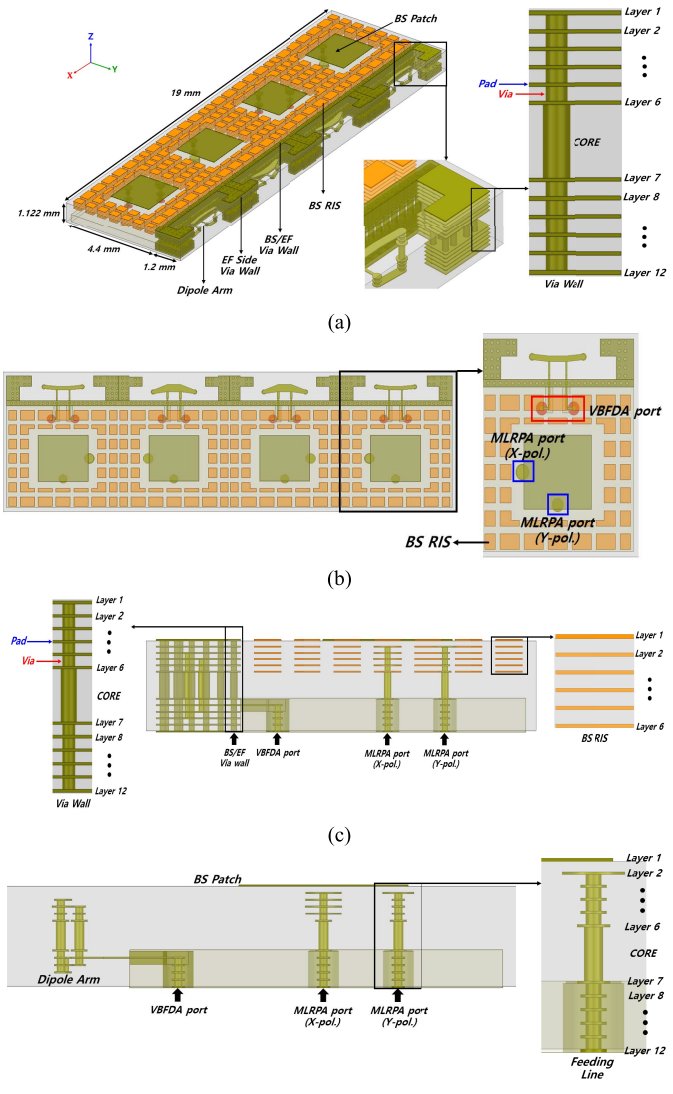

Fig. 2. Overview of the configuration naming and the overall dimensions of the proposed AiP. (a) Total view. (b) Top view. (c) Side view. (d) Side view w/o RIS and EF side via wall.

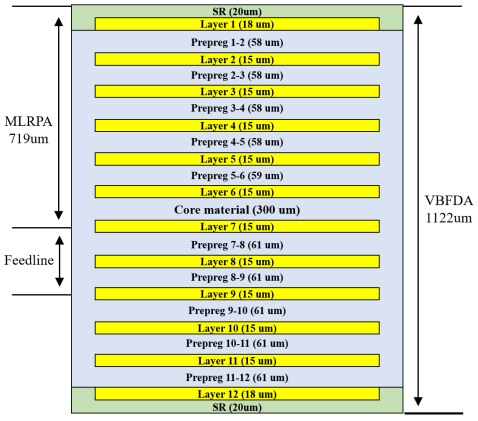

Fig. 3. Stack-up structure of the 12-layer PCB lamination.

and bottom ground. Unlike MLRPA, which requires a bottom ground, VBFDA can be designed by using whole layers of the stack-up structure. The feeds of the VBFDA are connected to the strip lines of layer 8. These strip lines are connected to the 16-channel radio frequency (RF) chip through layers 8 to 12. To measure the performance of the proposed antennas, the AiP is designed by connecting the feeds of MLRPA and VBFDA directly to layer 12 without going through the feedline layer. In the manufacturing process, there is a tolerance for a sawing line when dicing the substrate; thus, the proposed AiP was designed while considering a tolerance range of 0.15 mm. In addition, the copper ratio should be taken into consideration for the manufacturing process and the area of each layer should be filled with at least 30% copper. If there is less than 30% copper, the manufacturing error increases and the gap between the layers becomes distorted. When considering the aforementioned integration and fabrication factors for the full package level, the proposed AiP is verified by employing the active S parameters that can examine the level of isolation among the antenna elements in the arrays. The active S-parameters, which represent the reflection coefficients for various array excitations, are important performance parameters for active phase array antennas [15], [16]. The active S parameters are represented by the reflection coefficient for one port when another port is excited. Unlike the S parameter of a single antenna, the active S parameters for an array antenna are calculated for the coupling coefficient as well as the reflection coefficient.

III. MLRPA for the Broadside Array

Patch antennas have been widely investigated in 5G wireless communication systems since it has many advantages that include its low profile, small size, lightweight, ease of fabrication, and low cost [5]–[8]. As previously mentioned, the conventional patch antenna has the disadvantage of a narrow bandwidth. Since many applications require broadband, several methods for expanding the bandwidth are being studied. Typical methods to increase the bandwidth are to use air-filled substrates [17], parasitic elements [18], stack patches [19], patch-shaped modification [20], and thick substrates [21]. The air-filled substrate is not suitable for practical smartphones that require structural durability. Most of the parasitic element methods are also inappropriate because they are accompanied by a considerable increase in the overall size of the antenna. The remaining methods also have limitations in obtaining the desired bandwidth. Among them, the use of a thick substrate is the most practical way to increase the bandwidth and to avoid the disadvantages of the other methods as long as it does not cause a substantial loss due to a higher order of surface waves. The ideal substrate thickness is in the range of $\lambda_0/20$ to $\lambda_0/10$. As a result, the thickness (t) for 28 GHz is 0.535 mm $<$ t $<$ 1.07 mm and 39 GHz is 0.39 mm $<$ t $<$ 0.78 mm. As demonstrated in Fig. 3, the thickness of the MLRPA is identified by considering the aforementioned stack-up structure, which was determined to be 0.719 mm.

A. Patch Antenna With Disk Coupled Feed & RIS

The proposed design approach to achieve dual-band and dual-polarization operations with a small form factor start

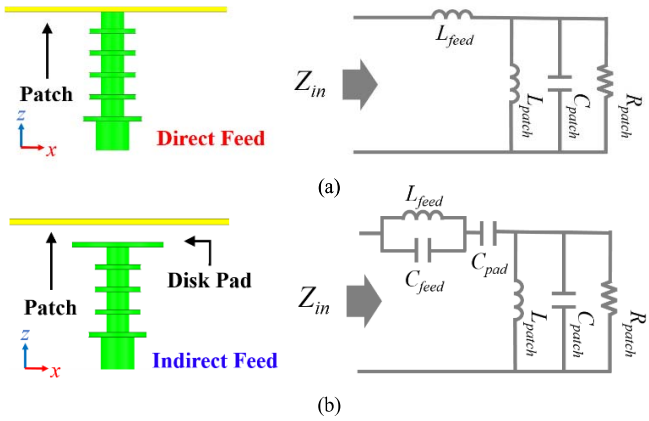

Fig. 4. Side view and equivalent circuit model of a patch antenna. (a) Conventional direct feed. (b) Indirect feed.

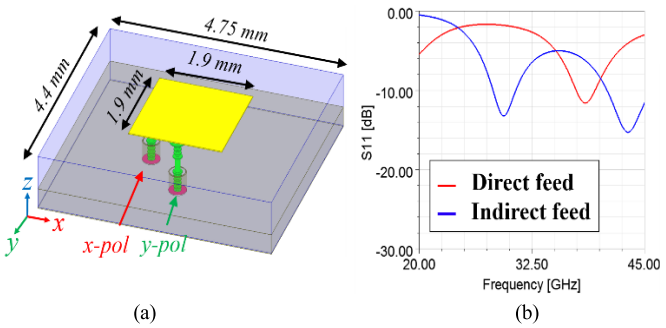

Fig. 5. (a) Topology of a single patch element and (b) its simulated S_{11} for direct and the proposed indirect feed (proximity disk coupled feed).

from modifying the shape of the patch element. The operation of the patch should be along the same direction as the polarization and it also needs to support dual-band impedance matching to the feed line. This is a critical bottleneck when trying to achieve dual-band and dual-polarization operations simultaneously. Dual-band and dual-polarized antennas have been studied in various manners, such as slot-loaded patch antennas, slotted cross-patch antennas [22], and conventional stack patch antennas [19]. In addition, another method is to modify the feed method, which can be combined with modified patch antennas as previously discussed. However, if the slots are applied to the patch to achieve dual-band operation for small-size substrates, the flow of electric current caused by the slots varies nonideally. As a result, it is challenging to support dual band and dual polarization simultaneously. In addition, the conventional stacked patch antennas can achieve dual band; however, their bandwidth is limited due to the given substrate thickness and the number of stacked layers. Therefore, in certain levels of small form factor, it can be more effective to modify the feed method than to modify the shape of the patch. Feed methods are largely classified into direct feed and indirect feed methods based on their physical connection topology. In the case of the direct feed method, physical contact is made to the radiating patch element. In the case of the indirect feed method, power is supplied by using single or multiple coupling effects at a certain distance from the radiating patch element.

Fig. 4(a) describes the direct feed when it is applied to a conventional patch antenna that has a thicker substrate. The design parameter to improve the impedance matching features is limited to a short segment of vertical inductance. Because of this limitation, it is more efficient to employ an indirect feed that can increase the design freedom significantly by maximizing the use of the coupling coefficients and the horizontal metallic patterns in each layer. The proximity feed [23], aperture coupled feed [24], L-shape proximity coupled feed [25], and the coplanar capacitive feed [26] are representative indirect feed methods. In this article, when considering the advantages and disadvantages of the methods, a novel proximity disk coupled feed method that combines the L-shaped feed and the coplanar capacitive feed is devised in Fig. 4(b). By changing the parameters of the diameter and height of the disk pad, the real and reactive parts of the antenna impedance can be tuned to significantly improve the bandwidth. The topology of the patch antenna with x- and y-polarization of the proximity disk is shown in Fig. 5(a). The dimensions of the patch and substrate are 1.9 mm × 1.9 mm and 4.4 mm × 4.75 mm, respectively. Fig. 5(b) shows an ordinary direct feed for the $\lambda_g/2$ microstrip antenna (where $\lambda_g = \lambda_0/\sqrt{\varepsilon_r}$, λ_0 = free-space wavelength and $\varepsilon_r = 3.47$), which has difficulty in achieving 28 and 39 GHz operations. On the other hand, a patch antenna with a proximity disk coupled feed placed on layer 2 can increase the design freedom in controlling the space of two resonant frequencies and their quality factor without changing the patch size or shape. Although a patch antenna with the novel feed method in Fig. 5 can support dual band and dual polarization for small-size substrates, the control range of the resonance frequency is still distant from the intended frequencies and the bandwidth needs to be further improved.

Applying a special structure to the antenna could improve its performance [27]. To broaden the bandwidth and to shift to the desired frequency, the tunable range of the input reactance can be extended by inserting a periodic RIS between the patch and the ground plane. RIS is also a known structure to have minimal interaction with a patch and greatly improve antenna characteristics such as the bandwidth and a miniaturized physical size [28]. As displayed in Figs. 6(a) and 7, a patch antenna with a single-layer RIS and the proximity disk coupled feed is simulated with the same antenna parameters as Fig. 5. Even if the upper frequency shifts down by optimizing the size and placement of the RIS, the bandwidth is still not enough. Unlike a single-layer RIS of the periodic structure that has been studied up to now, the reactance of the antenna has further enhanced the diversity in optimizing the impedance characteristics by changing the single-layer RIS into a double-layer RIS as depicted in Fig. 6(b). Its design capability of shifting down the resonance frequencies and widening the bandwidth are shown; however, the upper band responses are not enough for a 10 dB return-loss bandwidth of 3 GHz. It must be noted that for this design, each layer of the RIS has more than two different shapes and it is asymmetric, overlapping, or has multilayer patch elements. Although these nonuniform RIS designs can improve the bandwidth, significant nonuniformity in the multilayer RIS can cause the unintended degradation of the radiation patterns and gain due to nonuniform coupling

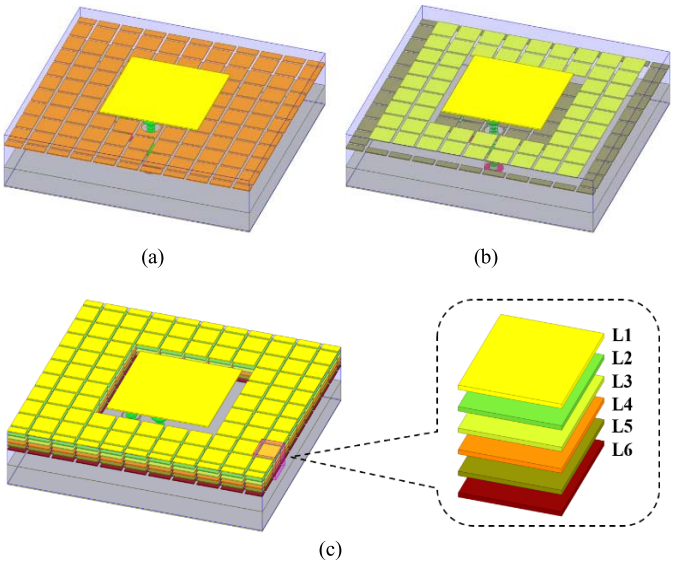

Fig. 6. Various types of RIS (a) single-layer (L4) RIS, (b) double-layer RIS (L3, L5), and (c) multilayer RIS (L1–L6).

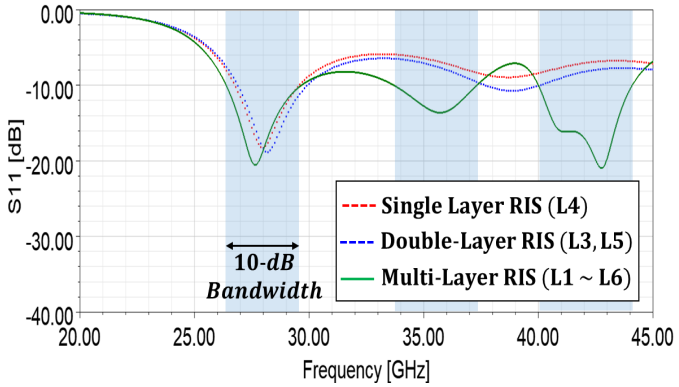

Fig. 7. Simulated S_{11} of single- and multilayer RIS as depicted in Fig. 6.

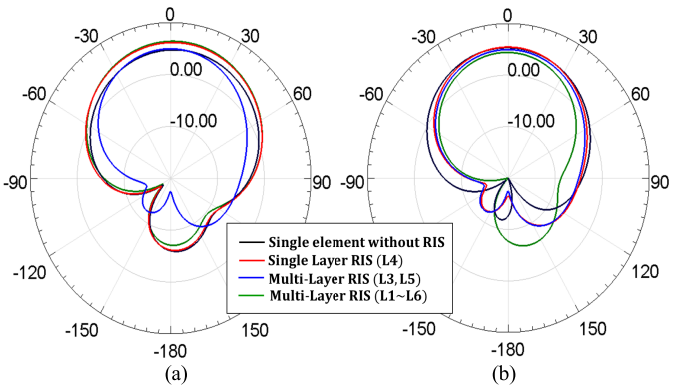

Fig. 8. Simulated yz-plane radiation patterns of a single-element patch antenna with and without single or multilayer RIS at (a) 28 GHz and (b) 39 GHz.

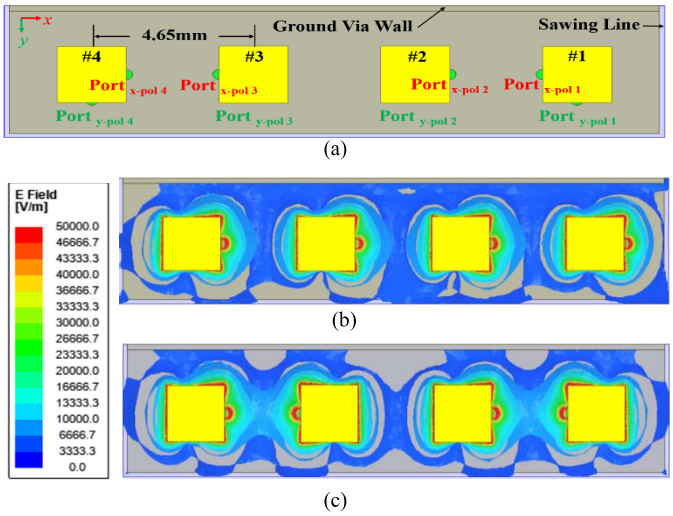

Fig. 9. (a) Top view of 1×4 MLRPA array. (b) Simulated E-field distributions for reference. (c) Optimized feed positions.

between each layer. Therefore, for the proposed topology, nonuniformity is employed only for the same plane. Fig. 6(c) illustrates a multilayer RIS that is arranged from layers 1 to 6. Fig. 7 shows the difference in the S parameter between the single-layer, the double-layer, and the multilayer RIS. The patch antenna with a single layer and a double layer cannot achieve a 10 dB bandwidth at the desired frequency; however, the multilayer RIS can achieve a wide bandwidth at the desired frequency.

In addition, Fig. 8 confirms that even if the RIS is added, the gain or radiation pattern does not change dramatically.

B. 1 × 4 *MLRPA Array*

In Section III-A, a single patch antenna with a multilayer RIS has been determined to be capable of dual-band and dual-polarization operations for 5G systems. Based on this, the 1 × 4 antenna array configuration is designed and optimized within the dimensions of 4.4 mm × 19 mm. To the best of our knowledge, this is the smallest AiP that can support dual band (28 and 39 GHz) and dual polarization for 5G smartphones.

As featured in Fig. 9(a), the MLRPA array consists of four antenna elements, four x-pol feeds, and four y-pol feeds. On one side of the antenna array that faces the proposed endfire array, VBFDA, there is a ground wall that isolates the operation of the MLRPA array from the VBFDA array, and the other three sides are surrounded by sawing lines for multiple fabrication samples. While the ideal patch antenna spacing of the array was set to $\lambda_0/2$ (=5.35 mm at 28 GHz), the 1 × 4 MLRPA array was arranged with an interval of 4.65 mm. This value of the interval is determined by the system set that means each of the elements of the smartphone has a definite place and space for being mounted. Samsung, a collaborative corporation, limits the maximum assigned space of antenna to 5 mm × 20 mm. Furthermore, proper operation in dual-band frequencies is also a design consideration. In free space, $\lambda_0/2$ of 28 GHz is 5.35 mm, $\lambda_0/2$ of 39 GHz is 3.84, and 4.6 mm is the median value of those two values. When an array antenna has a distance similar to the median value, authors consider that isolation of antenna performs well and grating lobe to not be generated in dual frequency bands. In summary, for the system set and performance of the antenna in dual frequency bands, the distance between two adjacent elements is determined to be 4.65 mm and this is a small size.

Because of its small size, the thick substrate, ground wall, and edges are very close to the patches. In addition, undesired surface waves flow along the substrate, which does not allow

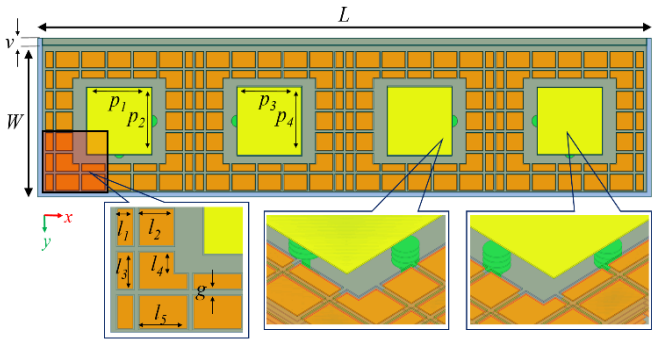

Fig. 10. Top and detailed views showing the topology and design parameters of 1 × 4 MLRPA array.

TABLE II
DESIGN PARAMETERS AND THEIR VALUES OF THE PROPOSED MLRPA. ALL PHYSICAL DIMENSIONS ARE IN mm

W / v	4.4 / 0.2	p_2	1.94	l_2	0.5
L	19	p_3	1.98	l_3	0.5
g	0.2	p_4	1.98	l_4	0.3
p_1	1.99	l_1	0.225	l_5	0.7

ideal radiation. The ground via wall physically blocks only one side of the array, which disrupts the symmetry of the AiP structure. In this study, since the surface wave effect was observed to be dominant along the longer axis, the ground via wall was strongly influenced with x-pol feeds rather than y-pol feeds. Fig. 9(b) shows the E-field distributions when the x-pol feeds of each antenna without the multilayer RIS are placed at the same position with respect to the patch. Since the E-field flows along the ground via wall, the wall causes an undesired influence on the bilateral patches. In Fig. 9(c), the x-pol feed position of antennas #2 and #4 is moved to the opposite end. In addition, it is given a phase difference of 180° to minimize the undesired effect on the bilateral patches. By modifying the position of the x-pol feeds, the influence between the bilateral patches and the ground via wall can decrease significantly.

As displayed in Fig. 10, since the substrate of the 1 × 4 MLRPA array is asymmetrically elongated in comparison to a single element, the RIS is also optimized such that it is long and asymmetric along the long axis. The RIS has the same shape when viewed in the quadrant of the entire antenna; thus, the RIS can uniformly affect each radiation patch. Table II shows the optimized dimensions of layers 1 to 6 for the MLRPA and the dimensions of RIS, which are the same for all of the layers. Because the distance between the patches is close and the substrate is small, the influence between the patches is much greater than the ideal 1 × 4 patch antenna array. For this reason, two patches at each end along the x-axis have slightly different dimensions from two patches near the center to achieve a 10 dB return-loss bandwidth for the active S parameter while considering the isolation. As shown in Fig. 10, adjusting the disk pad size of the feeds is one effective way to improve the additional bandwidth by adjusting the self-reactance and coupling coefficients. Fig. 11 illustrates the simulated 10 dB return-loss bandwidth of the proposed MLRPA array. The simulated 10 dB return-loss bandwidth for all of the ports was 26.59 to 29.74 GHz and

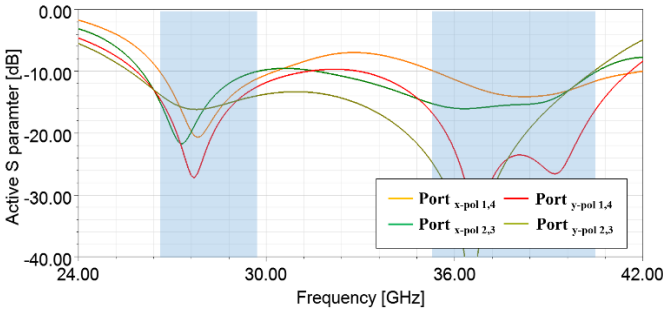

Fig. 11. Simulated active S parameter of the 1 × 4 MLRPA array.

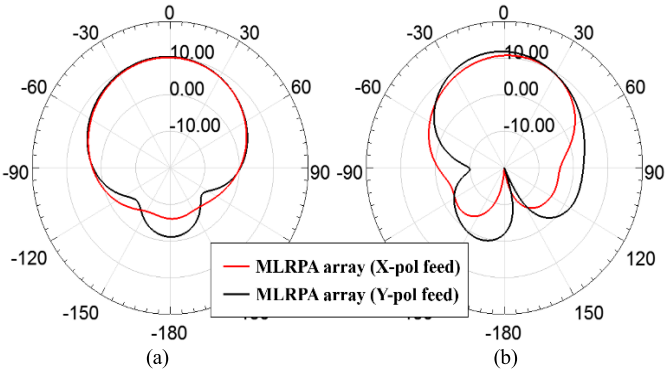

Fig. 12. Simulated radiation patterns of the 1 × 4 MLRPA array on the yz-plane at (a) 28 GHz and (b) 39 GHz.

35.33 to 40.42 GHz. Fig. 12 presents the simulated radiation patterns and gains of the 1 × 4 MLRPA that can achieve more than 10 dBi for all of the frequency bands and x- and y-pol feeds.

IV. VBFDA FOR ENDFIRE ARRAY

A. Single VBFDA

The design of the proposed endfire antenna array for target performance starts from the folded dipole antenna type. Similar to the MLRPA, a single VBFDA is a very small size with dimensions of 4.65 mm × 1.2 mm × 1.2 mm. Therefore, the conventional design approach for the folded dipole antenna type [10], [11] cannot achieve sufficient performance within the given space. There are various ways to overcome the limited space problem [29], [30]. In order to overcome the limitation of narrow space for dual-band operation, a dipole arm is vertically bent as shown in Fig. 13. It should be noted that for the endfire array design, only one polarization is considered with the aforementioned highly small form factor.

Unlike the conventional structure where the arms of the dipole antenna and the feed line are located on the same horizontal layer, the proposed VBFDA has a structure that is bent vertically. As a result, the dipole arms and feed line are located on different layers to save area. A single VBFDA uses two-port differential feeds. The ground via wall was placed for the isolation operation of the VBFDA from that of MLRPA as well as operating as a reflector for the VBFDA to achieve gain enhancement. Two-port differential feeds from a 50 Ω matched transmission line on layer 8 were connected to the dipole arm. The lower and upper arms of the VBFDA can be placed at various heights depending on the layer structure

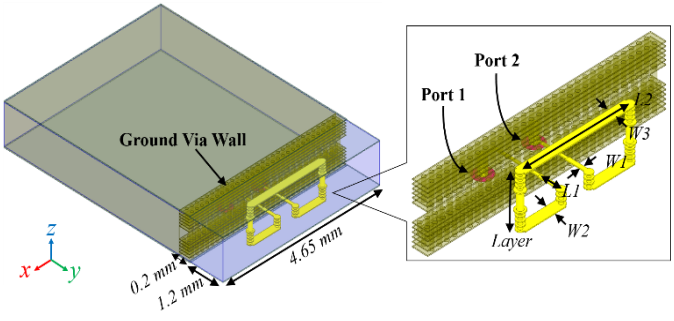

Fig. 13. Oblique views and dimension information for a single VBFDA.

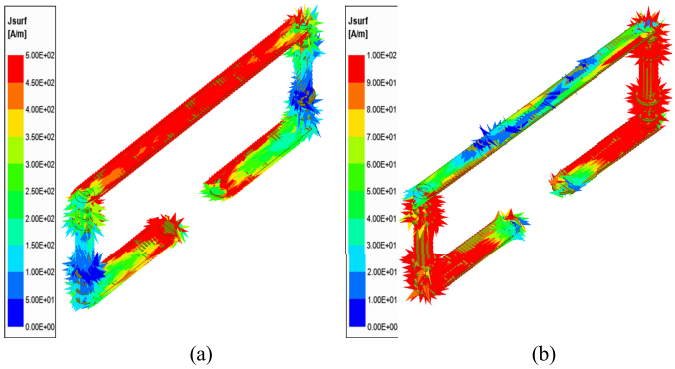

Fig. 14. Surface current distribution of the prototype single VBFDA at (a) 28 GHz and (b) 39 GHz.

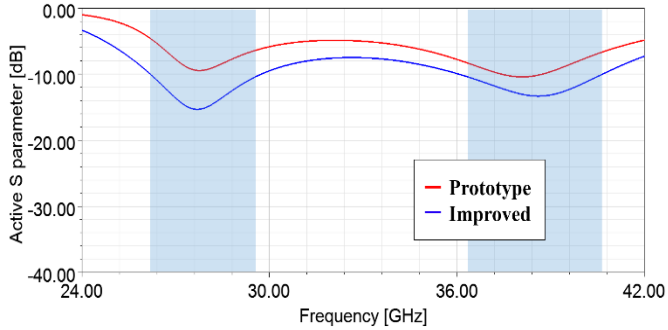

Fig. 15. Simulated active S parameter of the prototype and the improved single VBFDA.

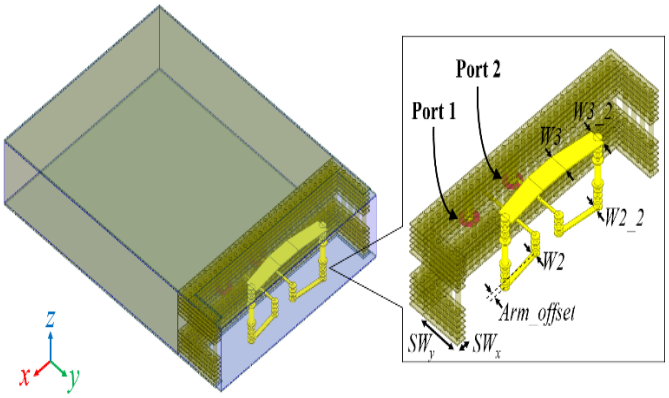

Fig. 16. Structure of the improved single VBFDA.

as demonstrated in Fig. 3. The lower and upper arms of the VBFDA have a width of W2 and W3, respectively, and the total length of the arm is L2, which is formed on both sides of the feed.

Fig. 14 shows the surface current distributions when the VBFDA operates with dual frequency bands. As depicted in Fig. 14(a), the electric current is strong in the upper and lower arms of the VBFDA at 28 GHz for two in-phase radiating elements. On the other hand, as displayed in Fig. 14(b), the electric current at 39 GHz is strong only in the lower arm. In this case, because one side of the lower arm has a length of $\lambda_{39\,\mathrm{GHz}}/4$, only the lower metallic traces operate as effectively as an open-ended half-wavelength dipole antenna at 39 GHz. It was also determined that the electric fields (E-fields) that radiated from both sides canceled each other out; thus, resulting in horizontal polarization. The proposed VBFDA can be designed at any two resonant frequencies according to the electrical length of each frequency band.

The red line of Fig. 15 shows the active S parameter that is obtained by optimizing the proposed VBFDA. It has a dual-band characteristic and can move the two resonant frequencies to the desired frequencies; however, the bandwidth is still narrow. It has not only a narrow bandwidth but also a low gain. Finally, in order to excite the enhanced performance of VBFDA, the shape of the VBFDA is changed as illustrated in Fig. 16. First, the folded dipole arm is transformed into a tapered shape with a different center and outer width. Unlike the previous one where the widths of the arms were the same at the beginning and the end, the improved antenna redefines the center width of the lower arm as W2 and the outer width as W2_2. In addition, the upper arm is redefined with a center width of W3 and an outer width of W3_2, respectively. The center width of the arm can be wider or narrower than the outside width through optimization. Second, an improved VBFDA applies a shape that is not parallel to the reflector, unlike a typical dipole antenna. As depicted in Fig. 16, the shape of the antenna may be bent so the distance between the inner pad center and outer pad center is the same as the arm offset. Therefore, the arm shape of the VBFDA can be folded forward or backward. Third, the method of placing the side via walls in order to add isolation effect on both sides of the VBFDA was considered. The proposed side via walls were built through all of the 12 layers by extending the ground via wall vertically. The vertical ground walls are placed on both sides of the VBFDA rendering an I-shaped array when observed from the top. The width of the side via walls should be wider than the minimum process size of the core pad. The side via walls are 200 μm away from the end of the substrate, which takes into account the sawing line that was previously mentioned.

The blue line of Fig. 15 shows the optimized active S parameter characteristics of the VBFDA with the side via wall, which satisfies a 10 dB return-loss bandwidth of 3 GHz for the target dual bands. Fig. 17 demonstrates that the gain of the proposed antenna has more than 3 dBi in the target band. In addition, the axial ratio of the VBFDA is more than 50 dB in the target band, which means that linear polarization is dominant.

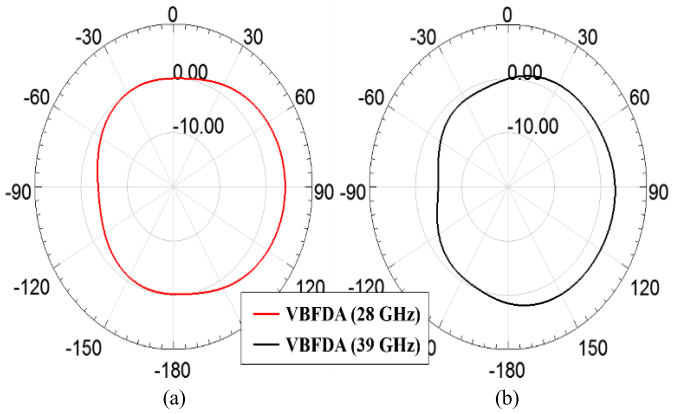

Fig. 17. Simulated yz-plane radiation patterns of a single VBFDA. (a) 28 GHz. (b) 39 GHz.

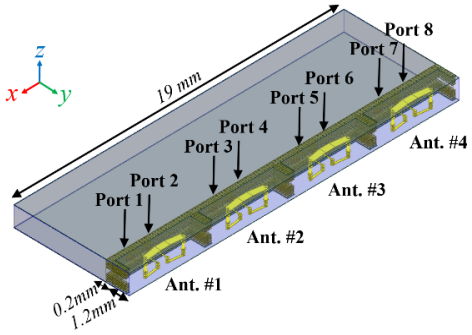

Fig. 18. Structure of the 1 × 4 VBFDA array having an I-shape side via wall.

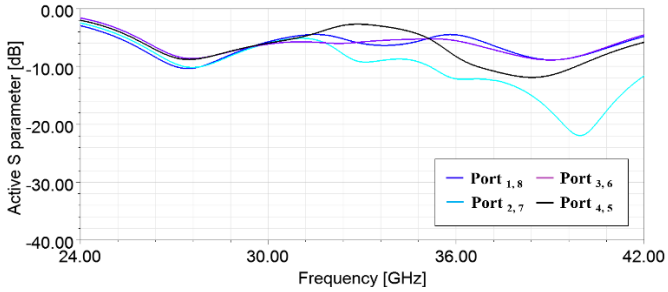

Fig. 19. Simulated active S-parameter of the 1 × 4 VBFDA array having an I-shaped side via wall.

B. 1 × 4 *VBFDA Array*

Fig. 18 shows the design of the 1 × 4 VBFDA array using the single element designed in Section IV. The y-axis length of the single antenna is 4.65 mm and the total length is 19 mm. Similar to the MLRPA, the spacing between each antenna is larger than $\lambda_{39\,\mathrm{GHz}}/2$; however, it is narrower than $\lambda_{28\,\mathrm{GHz}}/2$.

Isolation problems can occur with the designed antenna array. In order to consider the isolation characteristics between each element in the antenna array, the active S parameter should be checked as depicted in Fig. 19. While most ports are above −10 dB in the lower band, only some ports satisfy the condition below −10 dB in the upper band. Therefore, it can be expected that the isolation characteristics in the array are not good.

This problem can be accurately identified for the surface current distribution as shown in Fig. 20. Fig. 20 illustrates

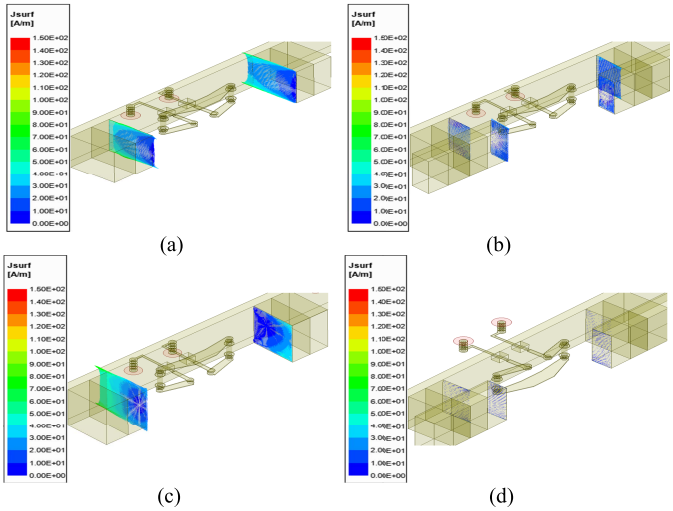

Fig. 20. Surface current distribution of the side via wall when the power is applied to only one antenna. (a) I-shape at 28 GHz. (b) T-shape at 28 GHz. (c) I-shape at 39 GHz. (d) T-shape at 39 GHz.

the current distribution when the power is not the applied antenna in this figure but adjacent antennas of this antenna. Fig. 20(a) and (b) show the current flow in I-shape and T-shape via wall region at 28 GHz, which is strong at I-shape via wall. Likewise, Fig. (c) and (d) show the current flow at 39 GHz, which is also strong at I-shape via wall. Therefore, in order to suppress the current flowing to both side antennas through the side via wall, it is necessary to modify the shape of the side via wall. As stated, Fig. 20(b) and (d) show the structure of a 1 × 4 antenna array with the shape of the side via walls modified from the I-type to the T-type for isolation characteristics. To prevent the power transfer to the other antenna through the side via wall, an x-axis wall was added at the end of the side via wall. The T-type side via wall structurally prevents the current from passing to the antennas on both sides and makes the current path long so that the current cannot pass easily. It can be observed from Fig. 20 that the T-type current decreases in comparison to the case of the I-type, and there is a significant difference, particularly at 39 GHz. Fig. 21(a) and (b) display the captured radial E-field of the I and T shape side via wall. Without the side via wall, a strong E-field is formed in the middle of the two antennas. Meanwhile, in the cases of I and T shapes, the null point gradually becomes apparent. This aspect can be observed for both bands. In addition, the intensity of the E-field propagating in the VBFDA is strong in the case of the T-shape. The tightly coupled effect between the VBFDA and the side via walls has a great effect on the antenna radiation.

Therefore, a 1 × 4 VBFDA array with the T-shaped side via walls can improve the isolation and gain characteristics as shown in Fig. 22. Similar to the MLRPA, two antennas at each end along the x-axis are structurally different from two antennas near the center; thus, the tapered shapes of the antennas achieve a 3 GHz bandwidth even though they are different. Table III shows the optimized geometric parameters of the VBFDA.

Fig. 23 presents the active S parameter of the 1 × 4 VBFDA array with the optimized T-shape side via wall. For the target

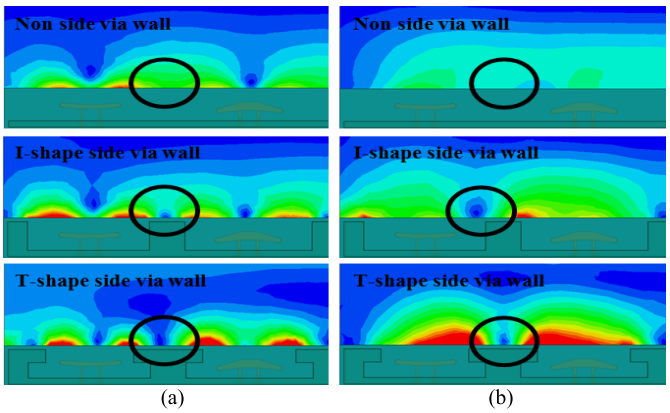

Fig. 21. E-field in the front space of the VBFDA depending on the side via wall shape at (a) 28 GHz and (b) 39 GHz.

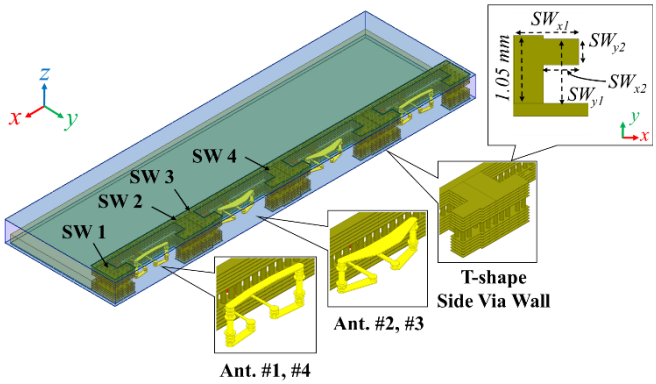

Fig. 22. Structure of the 1 × 4 VBFDA array with a T-shape side via wall.

TABLE III
DESIGN PARAMETERS AND THE VALUES OF THE PROPOSED VBFDA. ALL PHYSICAL DIMENSIONS ARE IN mm

Ant. 1				Ant. 2			
L1	0.435	$SW1_{x1}$	1.05	L1	0.445	$SW3_{x1}$	1.05
L2	0.541	$SW1_{x2}$	0.45	L2	0.613	$SW3_{x2}$	0.45
W1	0.05	$SW1_{y1}$	1.05	W1	0.09	$SW3_{y1}$	0.95
W2	0.15	$SW1_{y2}$	0.55	W2	0.2	$SW3_{y2}$	0.45
W2_2	0.15	$SW2_{x1}$	1.05	W2_2	0.15	$SW4_{x1}$	1.05
W3	0.15	$SW2_{x2}$	0.45	W3	0.3	$SW4_{x2}$	0.45
W3_2	0.15	$SW2_{y1}$	1.05	W3_2	0.15	$SW4_{y1}$	0.95
Layer	3L to 10L	$SW2_{y2}$	0.55	Layer	4L to 9L	$SW4_{y2}$	0.45
arm_offset		-0.05		arm_offset		0.16	

dual band, the bandwidth has more than 3 GHz and its isolation is less than −15 dB. Fig. 24 (a) and (b) show the yz-plane radiation pattern and gain at 28 and 39 GHz, respectively. The beam pattern of the VBFDA array is narrower than a single VBFDA, and the gain improved by 6 dB. As a result, the optimized 1 × 4 VBFDA array meets all of the requirements of the target band.

V. SIMULATION AND MEASUREMENT RESULTS

A. Simulation

In order to verify the design approaches of the MLRPA array and the VBFDA array of Section III-A, the proposed antennas were combined into the AiP and simulated with ANSYS HFSS v. 2019 R1. One of the design goals was miniaturizing the

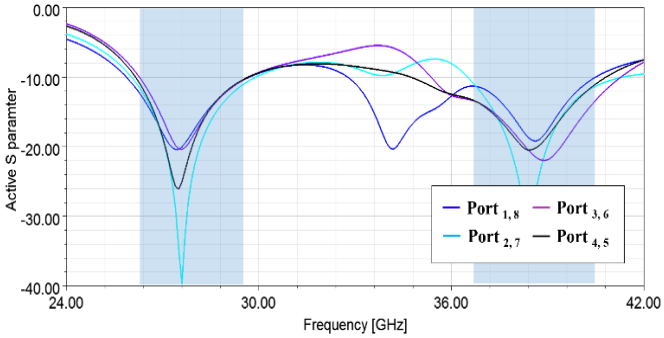

Fig. 23. Simulated active S-parameter of the 1 × 4 VBFDA array with a T-shape side via wall.

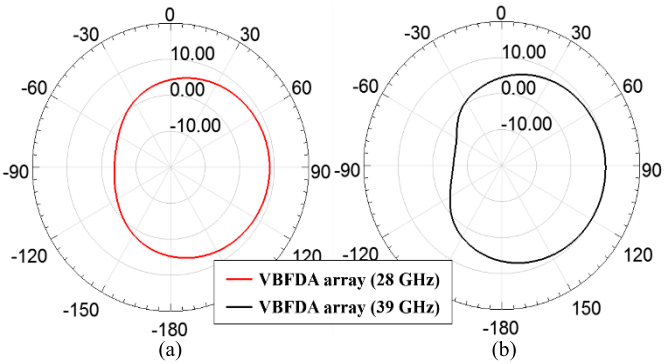

Fig. 24. Simulated yz-plane radiation patterns of the 1 × 4 VBFDA array for (a) 28 GHz and (b) 39 GHz.

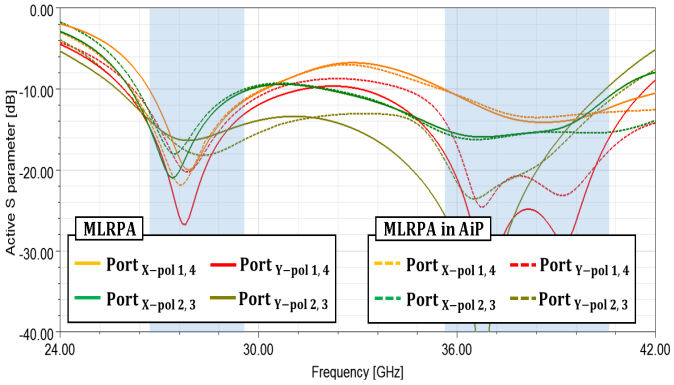

Fig. 25. Simulated active S parameter of the 1 × 4 MLRPA array in AiP.

antenna; hence, the size of the proposed AiP is 5.8 mm × 19 mm × 1.122 mm (0.54 λ_0 × 1.76 λ_0 × 0.105 λ_0, where λ_0 is the free-space wavelength at 28 GHz). As far as we know, the MLRPA array and the VBFDA array are the smallest in comparison to other designs and the combined AiP is also the smallest. Since both types of antennas are placed on a small substrate, the interference between the two antennas should be close to zero. Otherwise, the simulation results of the previous sections will be different from this section. The AiP combined with the MLRPA and the VBFDA is presented in Fig. 2 and was simulated.

Figs. 25 and 26 show the simulated active S parameter results of the MLRPA and the VBFDA in AiP. The 10 dB return-loss bandwidth of the MLRPA and the VBFDA is 26.22 to 29.57 GHz, 35.18 to 41.00 GHz, and 26.40 to 29.74 GHz, 36.65 to 40.72 GHz, respectively. Therefore, both

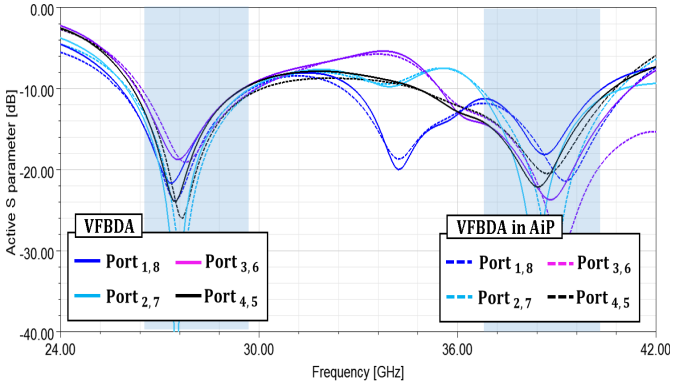

Fig. 26. Simulated active S parameter of the 1×4 VBFDA array in AiP.

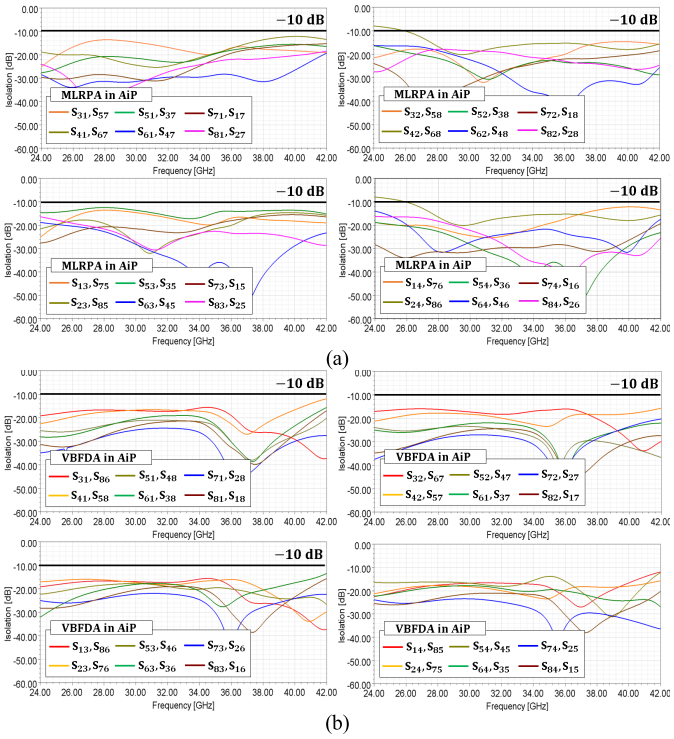

Fig. 27. Simulated isolation (a) 1×4 MLRPA array in AiP, (b) 1×4 VBFDA array in AiP.

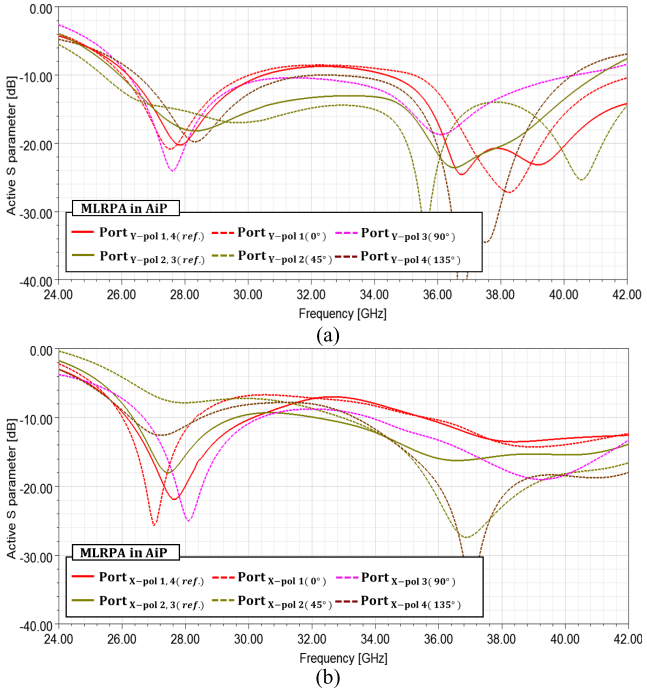

Fig. 28. Effect of phase difference on simulated active S parameter of the 1×4 MLRPA array in AiP. (a) Y-pol. (b) X-pol ports.

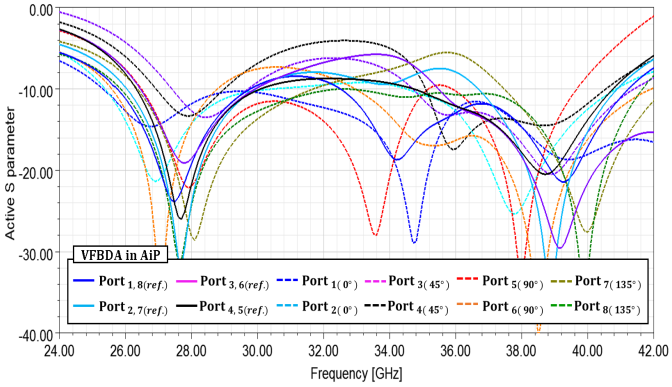

Fig. 29. Effect of phase difference on simulated active S parameter of the 1×4 VBFDA array in AiP.

antennas achieve more than 3 GHz for both bands, and the results for Sections III–V, which are represented by dashed lines and solid lines, do not differ significantly. This means that the isolation characteristics between the MLRPA and the VBFDA are good for the combined AiP structure.

Fig. 27 shows the simulated isolation results of MLRPA and VBFDA array in AiP, respectively. The simulated isolation results were less than −10 dB in almost all frequency bands. As the simulated isolation results of MLRPA and VBFDA were less than −10 dB, respectively, isolation between MLRPA and VBFDA was predicted to be less than −10 dB. Thus, the two arrays located within a very narrow space do not influence each other and they can operate independently.

Figs. 28 and 29 show the effect of phase difference on the active S parameter of MLRPA and VBFDA array in AiP. In these figures, solid lines represent the active S parameter in the condition that the phases of ports are all same. On the other hand, dash lines represent the active S parameter in the condition that phases of ports are different from each other. As phase difference changes active S parameter and bandwidth as above, antenna gain is expected to decrease while the beam is steered.

Figs. 30 and 31 represent simulated peak gain and efficiency results of MLRPA and VBFDA array in AiP. In operating frequency, the maximum peak gain of MLRPA and VBFDA array in AiP are 10.5/11.9 dBi (Y-pol MLRPA), 10.2/10.8 dBi (X-pol MLRPA), and 8.7/10 dBi (VBFDA). In addition, the efficiency of MLRPA and VBFDA array in AiP is more than 0.90 in operating frequency.

Fig. 32 displays the MLRPA's x-pol and y-pol radiation patterns in the yz-plane and xz-plane at 28/39 GHz, respectively. These results satisfy more than 10 dBi for the polarization and all of the frequencies whereas cross pol's gain in the yz-plane and xz-plane are extremely low compared with co pol's gain.

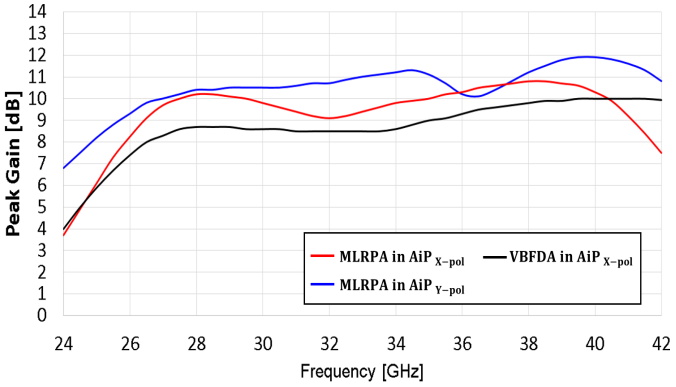

Fig. 30. Simulated peak gain of the 1×4 MLRPA and VBFDA array in AiP.

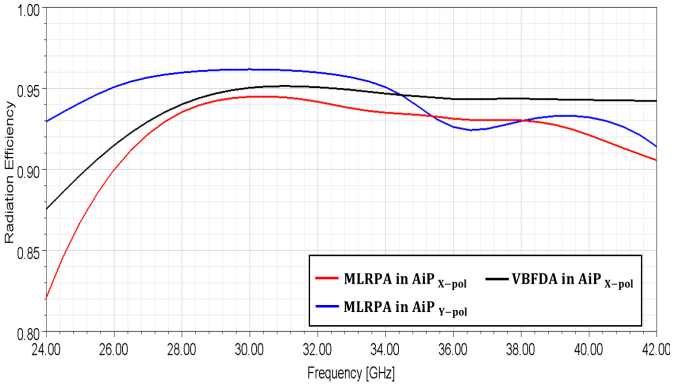

Fig. 31. Simulated efficiency of the 1×4 MLRPA and VBFDA array in AiP.

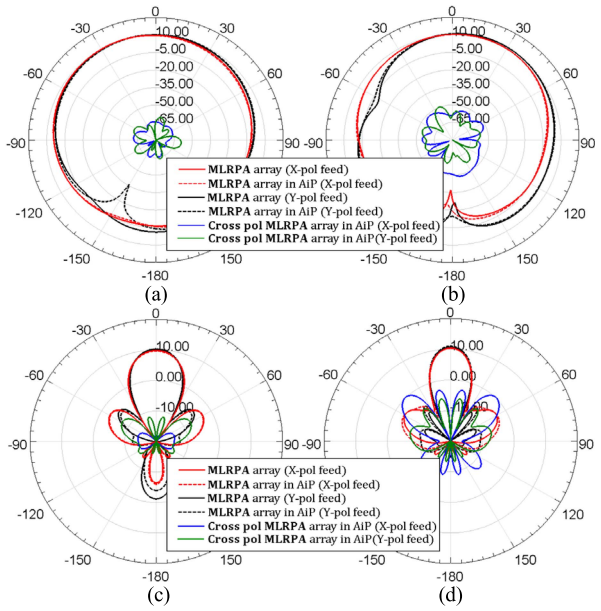

Fig. 32. Simulated radiation patterns of the 1×4 MLRPA array in AiP at (a) 28 GHz (yz-plane), (b) 39 GHz (yz-plane), (c) 28 GHz (xz-plane), and (d) 39 GHz (xz-plane).

In addition, the VBFDA's radiation patterns in the yz-plane and xz-plane at 28/39 GHz are presented in Fig. 33(a)–(d) and it satisfies more than 8 dBi for all frequencies whereas cross pol's gain in the yz-plane and xz-plane are extremely low compared with co pol's gain. Similar to the results of the bandwidth, the gain has a negligible difference between the results of Sections III–V. Even if the two antennas are

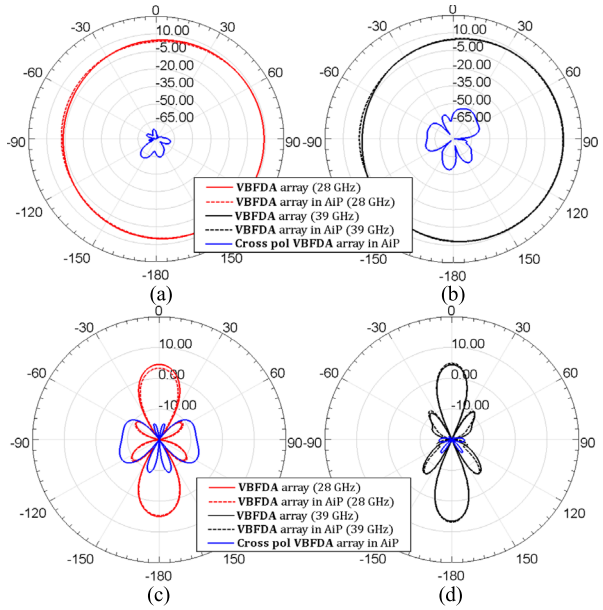

Fig. 33. Simulated radiation patterns of the 1×4 VBFDA array in AiP at (a) 28 GHz (yz-plane), (b) 39 GHz (yz-plane), (c) 28 GHz (xz-plane), and (d) 39 GHz (xz-plane).

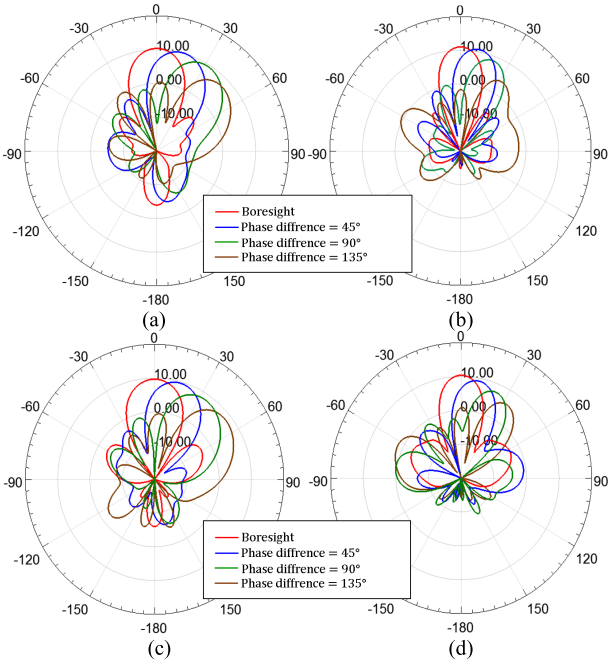

Fig. 34. Simulated beam steered radiation patterns (xz-plane) of the 1×4 MLRPA array in AiP at (a) 28 GHz (y-pol) (b) 39 GHz (y-pol), (c) 28 GHz (x-pol), and (d) 39 GHz (x-pol).

combined with AiP, the bandwidth and radiation pattern are not affected by each other and are unchanged as a result of their isolation characteristics.

Figs. 34 and 35 show simulated beam steered radiation patterns of 1×4 MLRPA and VBFDA array in AiP. Solid lines with red color represent boresight radiation pattern and the other solid line represents radiation pattern in the condition that phase differences of ports exist. The more beam is steered, the more peak gain is decreased. For instance, in Fig. 34(a), the peak gain of the steered beam is 10.36(boresight), 10.13(phase difference = 45°), 9.46(phase

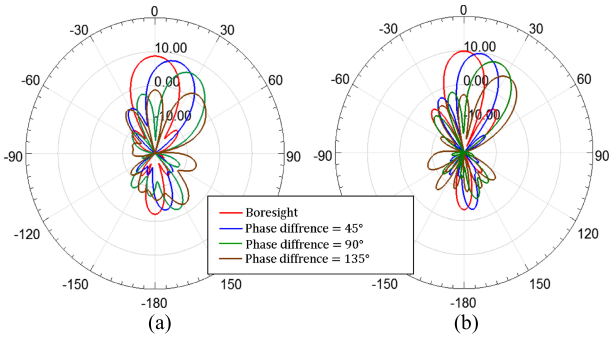

Fig. 35. Simulated beam steered radiation patterns (xz-plane) of the 1×4 VBFDA array in AiP at (a) 28 GHz (x-pol) and (b) 39 GHz (x-pol).

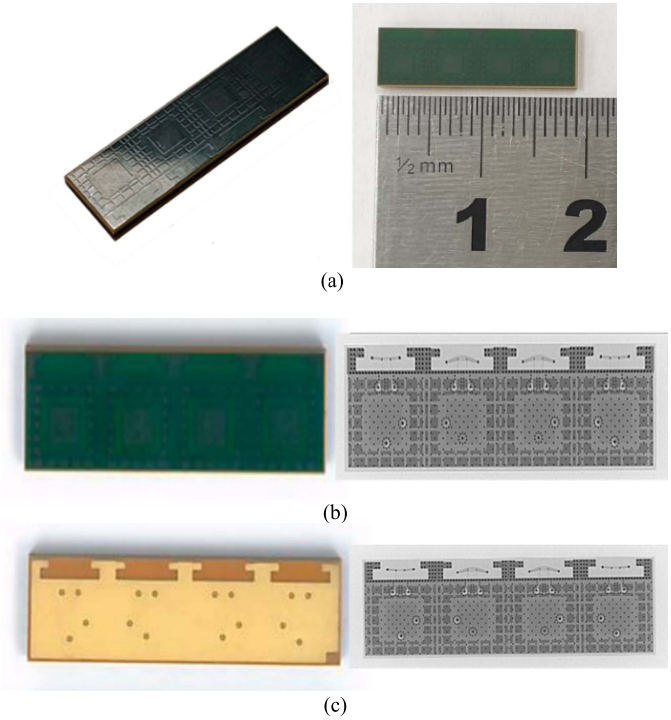

Fig. 36. Photograph and x-ray of the fabricated AiP depicted in Fig. 2. (a) Overall view. (b) Top view. (c) Bottom view.

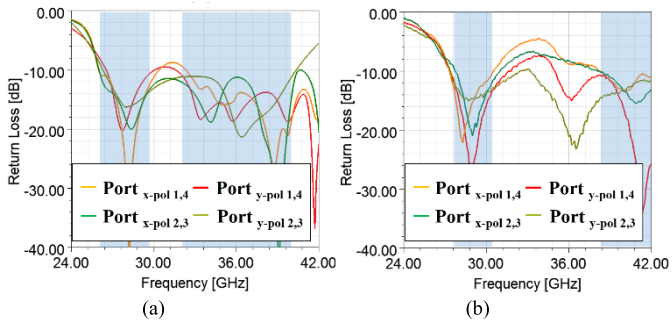

Fig. 37. Simulated and measured return loss of the MLRPA. (a) Simulation. (b) Measurement.

difference = 90°), 7.44 dBi (phase difference = 135°), respectively.

B. Reliability of Measurement

In order to fabricate and measure the AiP, the measurement systems need to be considered. As previously mentioned,

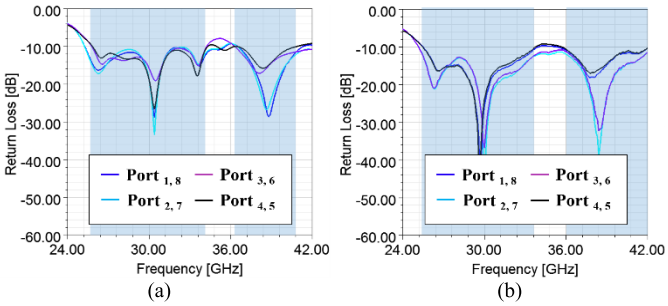

Fig. 38. Simulated and measured return loss of the VBFDA. (a) Simulation. (b) Measurement.

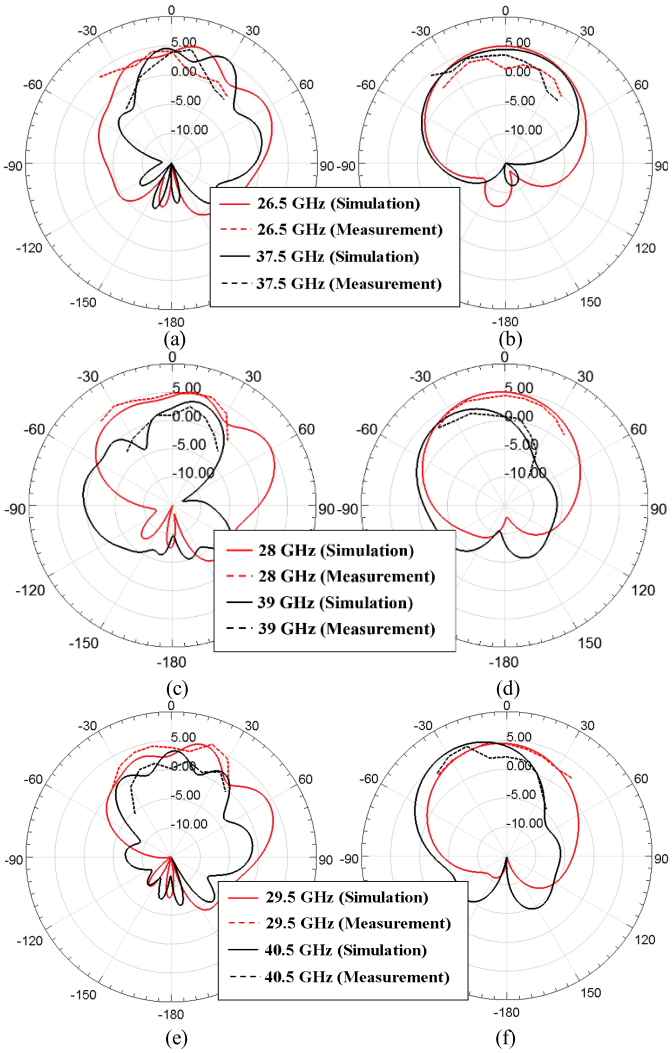

Fig. 39. Simulated and measured radiation patterns of MLRPA #1 x-pol [(a), (c), (e)] and (b) y-pol [(b), (d), (f)].

to measure the AiP without an RF chip, the feeds of a designed AiP were connected from the antenna to layer 12, which was directly connected to the probe of the vector network analyzer. The measurement system cannot measure all of the ports at once and it can only measure one port at a time. Therefore, the measurement results of each port are compared by one with the simulation results of each port. This HFSS simulation result is caused by the 50 ohm matching loads of all ports, except for one port that was used for

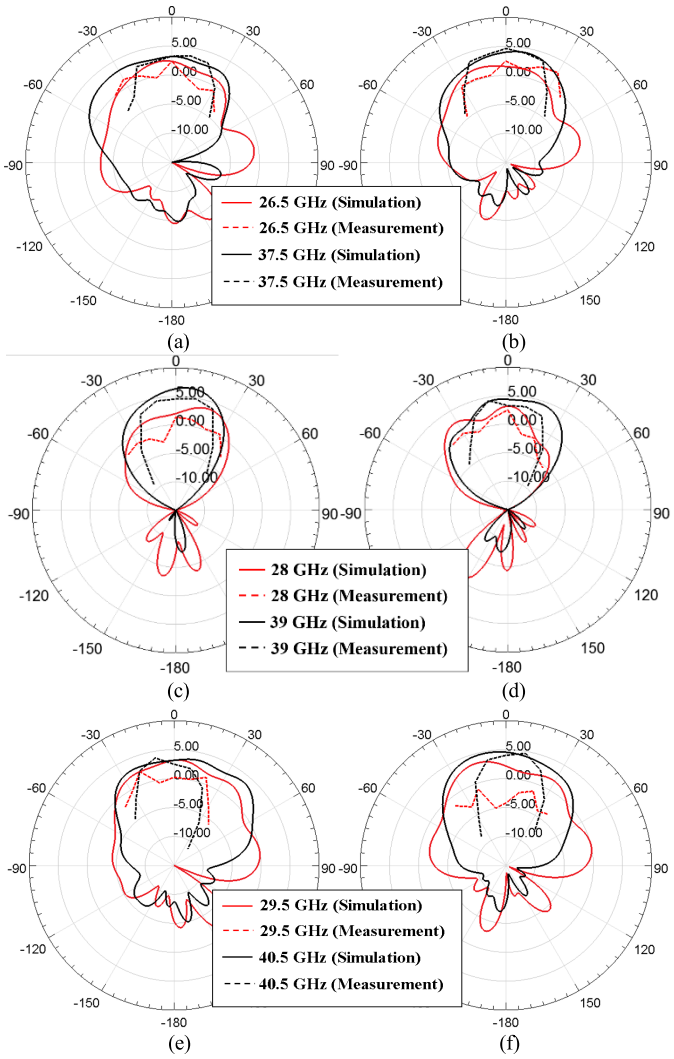

Fig. 40. Simulated and measured radiation patterns of VBFDA #1 [(a), (c), (e)] and #2 [(b), (d), (f)].

measurement. Due to the limitations of the RF chip and the measurement system, measurements were taken as previously described. If the simulation and measurement results for each port were similar, it was assumed that the simulation results in Sections III–V are the same as the actual measurement results for all of the ports.

C. Fabrication and Measurement Results

Fig. 36 shows the photograph and x-ray of the fabricated AiP with the S/R layer. Almost over 30% of the copper ratio is satisfied due to the ground via wall and the multilayer RIS placed on layers 1–6. The results of the HFSS simulations are compared with the results of the fabricated and measured AiP. Results of the MLRPA #1 antenna's x, y-pol, and VBFDA #1 and #2 antenna are presented in Figs. 37–40; the results of the other antennas are similar to these results. The 10 dB return-loss bandwidth results for the simulation and measurement of the MLRPA/VBFDA are depicted in Figs. 37 and 38, respectively.

The simulated 10 dB return-loss bandwidth of the MLRPA is 26.54 to 30.09 GHz, 32.31 to 40.36 GHz and the measured 10 dB return-loss bandwidth is 27.72 to 30.53 GHz, 38.21 to 42.00 GHz, respectively. The frequency band is slightly shifted to the upper band due to the alignment error of the multilayer RIS; however, the bandwidth is more than 3 GHz for both bands.

In the case of the VBFDA, the simulated 10 dB return-loss bandwidth is 25.84 to 34.25 GHz, and 36.51 to 40.92 GHz. The measured 10 dB return-loss bandwidth is 25.50 to 33.78 GHz, 35.63 to 42.00 GHz, respectively. These two results are not significantly different, and they have a bandwidth of 4.4 GHz or more for both bands. In Figs. 39 and 40, the simulated and measured radiation patterns of the MLRPA and the VBFDA are presented. The radiation patterns were measured for every 10° at 28/39 GHz and the measured shape of the radiation patterns and gain values are similar to the simulated results. Since the simulation results are similar to the measurement results, it can be assumed that the simulation results of the AiP in Section V are similar to those for the actual measurement results using the RF chip.

VI. Conclusion

A novel approach for a dual-band, dual-polarized, and miniaturized AiP for 5G smartphones is proposed. To the best of our knowledge, the smallest 5G smartphone AiP is composed of broadside and endfire antennas, which were designed to operate with dual band and dual polarization. The MLRPA achieved dual-band, dual-polarization, miniaturization, and broadband characteristics simultaneously by applying proximity disk coupled feed and multilayer asymmetric RIS techniques. In addition, the RIS helps to satisfy the 30% copper ratio at the same time as the performance of the antenna was increased. Because the structure of RIS is very complicated and the number of RIS layers is six, designing MLRPA was extremely hard and laborious work that required very long simulation time and trial and error. In addition, the small variation of elements such as the gap of RIS and size of patch changed impedance matching. Therefore, it was difficult to make MLRPA operated in dual frequency bands. The VBFDA achieved miniaturization by bending the existing folded dipole antenna vertically. The differential feed and the ground via wall improved the deteriorated gain due to miniaturization. In the case of the 1×4 antenna array, matching and isolation of the VBFDA were improved by using a side via wall structure. The proposed AiP is validated by the measurement results and it satisfies the specifications for mmWave 5G smartphones and mass production requirements. Therefore, it is expected to be able to mount an AiP with a mmWave 5G smartphone with the advantages of ultrasmall size, dual band, wide beam coverage, and high efficiency by using a single radiating element. This design is expected to be used for future studies related to 5G smartphone antenna technology.

References

[1] G. Gampala and C. J. Reddy, "Design of millimeter wave antenna arrays for 5G cellular applications using FEKO," in *Proc. IEEE/ACES Int. Conf. Wireless Inf. Technol. Syst. (ICWITS) Appl. Comput. Electromagn. (ACES)*, Mar. 2016, pp. 1–2.

[2] J. Helander, K. Zhao, Z. Ying, and D. Sjoberg, "Performance analysis of millimeter-wave phased array antennas in cellular handsets," *IEEE Antennas Wireless Propag. Lett.*, vol. 15, pp. 504–507, 2016.
[3] Y.-W. Hsu, T.-C. Huang, H.-S. Lin, and Y.-C. Lin, "Dual-polarized quasi Yagi–Uda antennas with endfire radiation for millimeter-wave MIMO terminals," *IEEE Trans. Antennas Propag.*, vol. 65, no. 12, pp. 6282–6289, Dec. 2017.
[4] *Qualcomm Extends 5G RF Leadership With New 5G Modules*. Accessed: Jul. 23, 2018. [Online]. Available: https://www.forbes.com/sites/moorinsights/2018/07/23/qualcomm-extends-5g-rf-leadership-with-new-5g-modules/#1753aa771c8d
[5] N. Ashraf, O. Haraz, M. A. Ashraf, and S. Alshebeili, "28/38-GHz dual-band millimeter wave SIW array antenna with EBG structures for 5G applications," in *Proc. Int. Conf. Inf. Commun. Technol. Res. (ICTRC)*, May 2015, pp. 5–8.
[6] T. Deckmyn, M. Cauwe, D. V. Ginste, H. Rogier, and S. Agneessens, "Dual-band (28,38) GHz coupled quarter-mode substrate-integrated waveguide antenna array for next-generation wireless systems," *IEEE Trans. Antennas Propag.*, vol. 67, no. 4, pp. 2405–2412, Apr. 2019.
[7] Y. Rahayu and M. I. Hidayat, "Design of 28/38 GHz dual-band triangular-shaped slot microstrip antenna array for 5G applications," in *Proc. 2nd Int. Conf. Telematics Future Gener. Netw. (TAFGEN)*, Jul. 2018, pp. 93–97.
[8] S. Lee, S. Kim, and J. Choi, "Dual-band dual-polarized proximity fed patch antenna for 28 GHz/39 GHz 5G millimeter-wave communications," in *Proc. 13th Eur. Conf. Antennas Propag. (EuCAP)*, Krakow, Poland, Mar. 2019, pp. 1–5.
[9] H. Ullah, F. A. Tahir, and Z. Ahmad, "A dual-band hexagon monopole antenna for 28 and 38 GHz millimeter-wave communications," in *Proc. IEEE Int. Symp. Antennas Propag. USNC/URSI Nat. Radio Sci. Meeting*, Jul. 2018, pp. 1215–1216.
[10] I. Syrytsin, S. Zhang, G. F. Pedersen, and A. S. Morris, "Compact quad-mode planar phased array with wideband for 5G mobile terminals," *IEEE Trans. Antennas Propag.*, vol. 66, no. 9, pp. 4648–4657, Sep. 2018.
[11] S. X. Ta, H. Choo, and I. Park, "Broadband printed-dipole antenna and its arrays for 5G applications," *IEEE Antennas Wireless Propag. Lett.*, vol. 16, pp. 2183–2186, 2017.
[12] R. A. Bijayeh, Z. H. Firouzeh, M. Maddahali, and I. Mazraeh-Fard, "Multi-band metamaterial-inspired miniaturized patch antenna using RIS," in *Proc. 24th Iranian Conf. Electr. Eng. (ICEE)*, May 2016, pp. 604–607.
[13] A. Mitra, S. Das, and A. Ghosh, "Design of modified reconfigurable RIS and its application in patch antenna miniaturization," in *Proc. IEEE Indian Antenna Week (IAW)*, Jun. 2016, pp. 51–54.
[14] P. Bhalekar, L. K. Ragha, and R. Gupta, "Wideband gap coupled microstrip antenna using RIS and RIS cavity resonator," in *Proc. 2nd IEEE Int. Conf. Recent Trends Electron., Inf. Commun. Technol. (RTEICT)*, May 2017, pp. 1291–1295.
[15] L. Lechtreck, "Cumulative coupling in antenna arrays," in *Proc. Antennas Propag. Soc. Int. Symp.*, Aug. 1965, p. 144.
[16] W. Kahn, "Active reflection coefficient and element efficiency in arbitrary antenna arrays," *IEEE Trans. Antennas Propag.*, vol. AP-17, no. 5, pp. 653–654, Sep. 1969.
[17] W. Abdel-Wahab, H. Al-Saedi, S. Safavi-Naeini, and Y. Wang, "SIW-integrated patch antenna backed air-filled cavity for 5G MMW appilcations," in *Proc. IEEE Int. Symp. Antennas Propag. (APSURSI)*, Jun. 2016, pp. 1233–1234.
[18] T. H. Jang, H. Y. Kim, I. S. Song, C. J. Lee, J. H. Lee, and C. S. Park, "A wideband aperture efficient 60-GHz series-fed E-shaped patch antenna array with copolarized parasitic patches," *IEEE Trans. Antennas Propag.*, vol. 64, no. 12, pp. 5518–5521, Dec. 2016.
[19] A. A. Serra, P. Nepa, G. Manara, G. Tribellini, and S. Cioci, "A wideband dual-polarized stacked patch antenna," *IEEE Antennas Wireless Propag. Lett.*, vol. 6, pp. 141–143, 2007.
[20] L. C. Ping, C. K. Chakrabarty, and R. A. Khan, "Design of ultra wideband slotted microstrip patch antenna," in *Proc. IEEE 9th Malaysia Int. Conf. Commun. (MICC)*, Dec. 2009, pp. 41–45.
[21] J. M. Kovitz and Y. Rahmat-Samii, "Using thick substrates and capacitive probe compensation to enhance the bandwidth of traditional CP patch antennas," *IEEE Trans. Antennas Propag.*, vol. 62, no. 10, pp. 4970–4979, Oct. 2014.
[22] P. Piazzesi, S. Maci, and G. Biffi, "Dual-band, dual-polarized patch antennas," *Int. J. Microw. Millim. Wave Comput. Aided Eng.*, vol. 5, no. 6, pp. 375–384, 2007.
[23] M. Veysi, M. Kamyab, and A. Jafargholi, "Single-feed dual-band dual-linearly-polarized proximity-coupled patch antenna," *IEEE Antennas Propag. Mag.*, vol. 53, no. 1, pp. 90–96, Feb. 2011.
[24] Q. Rao and R. H. Johnston, "Modified aperture coupled microstrip antenna," *IEEE Trans. Antennas Propag.*, vol. 52, no. 12, pp. 3397–3401, Dec. 2004.
[25] W. Lin and H. Wong, "Multipolarization-reconfigurable circular patch antenna with L-shaped probes," *IEEE Antennas Wireless Propag. Lett.*, vol. 16, pp. 1549–1552, 2017.
[26] G. Mayhew-Ridgers, J. W. Odendaal, and J. Joubert, "Efficient full-wave modeling of patch antenna arrays with new single-layer capacitive feed probes," *IEEE Trans. Antennas Propag.*, vol. 53, no. 10, pp. 3219–3228, Oct. 2005.
[27] W. Sun, Y. Li, L. Chang, H. Li, X. Qin, and H. Wang, "Dual-band dual-polarized microstrip antenna array using double-layer gridded patches for 5G millimeter-wave applications," *IEEE Trans. Antennas Propag.*, early access, Apr. 6, 2021, doi: 10.1109/TAP.2021.3070185.
[28] K. Buell, D. Cruickshank, H. Mosallaei, and K. Sarabandi, "Patch antenna over RIS substrate: A novel miniaturized wideband planar antenna design," in *Proc. IEEE Antennas Propag. Soc. Int. Symp., Digest. Held Conjunct With, USNC/CNC/URSI North Amer. Radio Sci. Meeting*, Jun. 2003, pp. 269–272.
[29] J. Wang *et al.*, "A low-profile vertically polarized magneto-electric monopole antenna with a 60% bandwidth for millimeter-wave applications," *IEEE Trans. Antennas Propag.*, vol. 69, no. 1, pp. 3–13, Jan. 2021.
[30] X. Dai, A. Li, and K. M. Luk, "A wideband compact magneto-electric dipole antenna fed by SICL for millimeter wave applications," *IEEE Trans. Antennas Propag.*, early access, Feb. 24, 2021, doi: 10.1109/TAP.2021.3060146.

Jungwoo Seo received the B.S. degree in electronics engineering from Inha University, Incheon, South Korea, in 2017, and the M.S. degree in electrical and computer engineering from Seoul National University, Seoul, South Korea, in 2020.

His research areas of interest includes smartphone antennas of 4G/5G communication.

Inseop Yoon (Member, IEEE) received the B.S. degree in electronics engineering from Korea Polytechnic University, Siheung, South Korea, in 2011, and the M.S. and Ph.D. degrees in electronics engineering from Inha University, Incheon, South Korea, in 2013 and 2019, respectively.

He is currently a Staff Engineer with Research and Development Team, Networks Business, Samsung Electronics, Suwon, South Korea. His current research interests include millimeter-wave antennas design for 5G communication and lens antenna, transmit array.

Jaebaek Jung (Member, IEEE) received the B.S. degree in electronic and electrical engineering from the Pohang University of Science and Technology (POSTECH), Pohang, South Korea, in 2012. He is currently pursuing the integrated master's and Ph.D. degree with the Department of Electrical Engineering and Computer Science, Seoul National University, Seoul, South Korea.

His main research interests are mmWave 5G antenna, 6G antenna, metasurface, and antenna in package.

Jeongki Ryoo received the Ph.D. degree in electronic engineering from Chungnam National University, Daejeon, South Korea, in 2004.

He is currently a Principle Engineer with Samsung Electro-Mechanics, Suwon, South Korea. His current research interests include 5G mmWave antenna and module design based on advanced antenna structure.

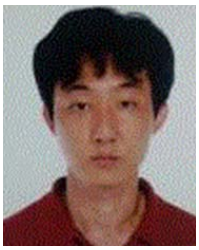

Juhyoung Park received the B.S. degree in electrical engineering from Yonsei University, Seoul, South Korea, in 2001.

He is currently a Principal Engineer with Samsung Electro-Mechanics, Suwon, South Korea. His research interests include 5G millimeter-wave antenna and module design.

Woncheol Lee (Member, IEEE) received the B.S. degree in computer engineering from Yeungnam University, Gyeongsan, South Korea, in 2007, and the M.S. and Ph.D. degrees in electrical engineering from The University of Alabama, Tuscaloosa, AL, USA, in 2012 and 2017, respectively.

In 2018, he was a Postdoctoral Research Fellow with the NSF Industry/University Cooperative Research Center-The University of Alabama (IUCRC-UA): Center for Efficient Vehicles and Sustainable Transportation System, The University of Alabama. He is currently a Staff Engineer with Samsung Electro-Mechanics, Suwon, South Korea. His research interests include 5G millimeter-wave antenna and module design, magnetic materials for RF devices, and the design of magnetodielectric-loaded RF devices.

Dongok Ko received the B.S. and M.S. degrees in radiowave engineering from Chungnam National University, Daejeon, South Korea, in 2015 and 2018, respectively.

He is currently an Engineer with Samsung Electro-Mechanics, Suwon, South Korea. His research interests include 5G millimeter-wave antenna and module design.

Jungsuek Oh (Senior Member, IEEE) received B.S. and M.S. degrees from Seoul National University, Seoul, South Korea, in 2002 and 2007, respectively, and the Ph.D. degree from the University of Michigan at Ann Arbor, Ann Arbor, MI, USA, in 2012.

From 2007 to 2012, he was with Korea Telecom, Seoul, as a Hardware Research Engineer, working on the development of flexible RF devices. From 2013 to 2014, he was a Staff RF Engineer with Samsung Research America, Dallas, TX, USA, working as a Project Leader for the 5G/millimeter-wave antenna system. From 2015 to 2018, he was a Faculty Member with the Department of Electronic Engineering, Inha University, Incheon, South Korea. He is currently an Associate Professor with the School of Electrical and Computer Engineering, Seoul National University. He has published more than 50 technical articles. His research areas include mmWave/THz beam focusing/shaping techniques, antenna miniaturization for integrated systems, and radio propagation modeling for indoor scenarios.

Dr. Oh has served as a Technical Program Committee (TPC) Member. He was a recipient of the 2011 Rackham Predoctoral Fellowship Award at the University of Michigan, the 2018 SNU Creative-Pioneering Research Award, and the 2019 IEEE AP-S/Microwave Theory and Techniques (MTT) Seoul Chapter Best Paper Award. He has served as a Session Chair for the IEEE AP-S/USNC-URSI and the International Symposium on Antennas and Propagation (ISAP). He has been an Associate Editor for *Microwave and Optical Technology Letters* and *ICT Express*.